Surface & Coatings Technology 421 (2021) 127359

Contents lists available at ScienceDirect

Surface & Coatings Technology

journal homepage: www.elsevier.com/locate/surfcoat

Mechanical performance and residual stress of WC-Co coatings manufactured by Kinetic Metallization™

Ashok Meghwal [a], Christopher C. Berndt [a], Vladimir Luzin [b,c], Christiane Schulz [d,e], Travis Crowe [f], Howard Gabel [f], Andrew S.M. Ang [a,*]

[a] Surface Engineering for Advanced Materials (SEAM), Swinburne University of Technology, Hawthorn, VIC 3122, Australia
[b] Australian Nuclear Science & Technology Organisation (ANSTO), Lucas Heights, NSW 2234, Australia
[c] School of Engineering, The University of Newcastle, Callaghan, NSW 2308, Australia
[d] Future Industries Institute, University of South Australia, Mawson Lakes Campus, SA 5000, Australia
[e] Surface Engineering for Advanced Materials (SEAM), University of South Australia, Mawson Lakes Campus, SA 5000, Australia
[f] Inovati, 1501 Cook Place, Santa Barbara, CA 93117, USA

ARTICLE INFO

Keywords:
WC-Co
Kinetic metallization
Mechanical properties
Residual stress
Wear

ABSTRACT

Electrolytic hard chrome (EHC) plating is a source of environmental pollution due to evolution of hexavalent chromium, which is a known carcinogen. Coating technology known as Kinetic Metallization™ (KM™) is an alternative to EHC for depositing wear resistant WC-Co coatings. Kinetic Metallization™ employs high kinetic energy of impacted feedstock particles and achieves a dense coating with good intersplat bonding. However, the high kinetic energy imparts peening and thermal stresses that are different from other thermal spray processes. This work characterizes the residual stress profile and room temperature wear behaviour of WC-Co coatings deposited under several input parameters. A combination of SEM imaging and etched optical micrographs revealed significant plastic deformation and particle penetration at the interface due to high energy impact of feedstock particles. No signs of substrate grain refinement were detected. The coating was composed primarily of WC and Co with minor compositional variations, as calculated by quantitative Rietveld analysis, with respect to the input parameters. Coating residual stresses were compressive in nature due to domination of thermal contraction stresses over peening stresses. The wear resistance assessed by the pin-on-disk method revealed a wear performance equivalent to conventionally sprayed WC-Co coatings.

1. Introduction

Electrolytic hard chrome (EHC) plating is used in industry due to its high-performance capabilities in providing superior hardness, wear resistance and corrosion resistance for protecting components in high wear environments. However, EHC has an uncertain future as legislation concerning hexavalent chromium, a known carcinogen, becomes more stringent and restrictive due to its hazardous health and environmental effects. An alternative approach is to employ cold spray (CS) nanostructured tungsten carbide cobalt (WC-Co) coatings [1] that have exhibited positive outcomes in wear applications. Hence this work explores a variant CS process called Kinetic Metallization™ (KM™) [2] for deposition of WC-Co coatings.

Traditionally, WC-Co coatings are applied to surfaces by combustion or electrical thermal spray processes; including flame spray, detonation spray (DS), high velocity oxygen fuel (HVOF) and atmospheric plasma spray (APS) [3]. These methods require control of processing parameters to achieve a uniformly dense coating. Often these high temperature environments and rapid solidification processes also result in undesirable features in coatings. These coating defects include multi-phase formation in the coating, porosity, a void network and detrimental residual stress [4].

On the other hand, impact consolidation methods of cold spray and KM™ prevent unfavorable thermal input and rely on solid state cold welding technique as bonding mechanism arising from plastic deformation [5,6]. All of the Cold Spray variants rely on the injection of metal particles into a supersonic stream of accelerant gas. The KM™ design features a patented friction compensated sonic nozzle to accelerate

* Corresponding author at: Faculty of Science, Engineering and Technology, Department of Mechanical Engineering and Product Design Engineering, Surface Engineering for Advanced Materials (SEAM), Swinburne University of Technology, H38, P.O. Box 218, Hawthorn, VIC 3122, Australia.
E-mail address: aang@swin.edu.au (A.S.M. Ang).

https://doi.org/10.1016/j.surfcoat.2021.127359
Received 12 January 2021; Received in revised form 5 May 2021; Accepted 23 May 2021
Available online 28 May 2021

particles [7]. In the KM™ process, thermally soften powder particles (from 1 to 50 μm in diameter) are accelerated to sonic velocities of 500 to 1500 m/s by a gas jet through a friction-compensated sonic nozzle [2]. The nozzle design restricts the gas flow below Mach 1, leading to equal gas density past the nozzle throat; thereby averting any losses associated with kinetic energy of the particles [2,8]. The high velocity particles convert their kinetic energy to mechanical and thermal deformation so that they adhere to the underlying material and form a dense and oxide free coating by a process similar to explosive welding. The low process temperature avoids decarburization and oxidation of the WC-Co [7].

Conventional WC-Co based composite coatings are composed of high proportions of hard WC phase of up to 80 wt% in conjunction with low amounts of Co as the binder material. The WC component enhances the hardness and wear resistance of the coatings, while, the Co binder improves the toughness of the composite [1,9]. Hence, the wear resistance of the WC-Co coating system will decrease with an increase in the binder content. Thus, research on these composite coatings has focused on high WC content to further improve the wear resistance [10,11]. However, the current work on KM™ WC-Co coatings employed high Co content to investigate this specific process and the influence of high binder content on the overall wear resistance. The wear behaviour of KM™ WC-Co coating with high binder content was studied under dry sliding conditions using a pin-on-disk method against an alumina ball. The morphology, structure and composition of the worn surface were assessed to understand the wear mechanism.

Specific knowledge on the magnitudes of peening and thermal stress, which together evolve the residual stress profile of the KM™ WC-Co coatings, is needed for comparison purposes to other cold spray and HVOF technologies. These coating systems are used in critical applications such as landing gear pistons and axle journals, hydraulic rods, engine shaft journals, and other components that operate under high cycle conditions. The residual stress state developed during any coating process has a significant influence on fatigue properties.

Hence, knowledge of stresses and their linkage to other properties and production parameters is essential for these critical structures. WC-Co coatings were prepared under a two-factorial design that involved the process gas pressure and gas temperature. Relationships among (i) processing conditions, (ii) microstructure, (iii) residual stresses, and (iv) the mechanical properties of these coatings were investigated.

2. Experimental details

2.1. Coating procedure

The Kinetic Metallization™ system (Inovati, Santa Barbara, CA 93117, USA) consists of a KM™ Gun, a control cabinet with dual powder fluidizing units, and a fully enclosed spray cabinet. The patented KM™ Gun [12,13] has a friction compensated sonic nozzle with an integrated gas heater and combined powder injection and mixing chamber. The powder particles that pass through this nozzle are typically accelerated to speeds up to 1000 m/s, which are then deposited onto a substrate to form a coating.

Helium was used as an accelerant gas for the current KM™ system. Gas temperature and pressure were varied in this study since these variables largely influence the coating deposition. The inlet gas pressures were between 0.414 and 0.621 MPa (60–90 psi) and gas temperature were 760–980 °C (1400–1800 °F). Three coatings were fabricated onto a SAE1018 mild steel substrate (3.0 mm thick) with the KM™ parameters (i) 0.414 MPa and 760 °C (60 psi and 1400 °F), (ii) 0.414 MPa and 980 °C (60 psi and 1800 °F), and (iii) 0.621 MPa and 760 °C (90 psi and 1400 °F). Identical samples at each parameter setting were procured for neutron measurements and to perform metallography, SEM, instrumented indentation, and wear testing.

2.2. Microstructural and mechanical characterization

The coated substrates were metallurgically prepared in accordance to the ASTM E1920: Standard Guide for Metallographic Preparation of Thermal Sprayed Coating [14]. Microscopy and image analysis (IA) using Image J® (National Institute of Health, USA) allowed quantitative measurements of coating porosity. Cross-sections of the coating microstructure were characterized using a field emission scanning electron microscope (SEM) (Zeiss SUPRA™ 40VP FESEM system) with a working voltage of 20 kV and working distance of 10 mm. An energy dispersive X-ray spectrometer EDS (Oxford Instruments, INCAxcat detector) was adopted for point scanning of element distributions. Bruker's D8 discover powder X-ray diffraction (XRD) system (Bruker Corp., Billerica, MA, USA) was used for phase analysis of the coatings. The samples were scanned under Cu Kα radiation over a 2θ range of 30° to 90° at a voltage of 40 kV, a current of 30 mA and a 0.05°2θ step size. Quantitative Rietveld analysis was performed using DIFFRAC.SUITE TOPAS 4.2 (Bruker Corp., Billerica, MA, USA) interface to calculate the carbide and cobalt contents in coatings. The diffraction patterns for KM™ WC-Co coatings include complex phases that obscure peak fitting. Hence, the Rietveld analysis is a guide towards changes in the coating composition under different input parameters.

The microhardness evaluation of the coating cross section was performed according to ASTM C1327: Standard Test Method for Vickers Indentation Hardness of Advanced Ceramics [15], using the Hysitron TI 980 Triboindenter indentation platform (Bruker Corp., Minneapolis, MN). Indents were set at a load of 3 N and at least 20 indents were performed on each coating. The indenter records the applied load and penetration depth for the loading and unloading cycle. Hardness is calculated by dividing the maximum load on the load-displacement curve by the area of the indent. The elastic modulus was determined by using the Oliver-Pharr method from the slope of the unloading curve shown on the load-displacement graph [16].

2.3. Residual stress analysis

All substrates of SAE1018 mild steel (3.0 mm thick) underwent stress relief at 500 °C for 3 h. Then, the substrates were lightly blasted with SiC grit to remove any oxide scales as well as any surface irregularities such as scratches or gouges. Prior to deposition, the coated side was high pressure grit blasted with boron carbide. These steps ensured that all the substrates were at similar initial stress states so that valid comparisons could ensue after the neutron measurements. Residual stresses were measured by a neutron diffraction technique using KOWARI, the neutron residual stress diffractometer at the Australian Center for Neutron Scattering (ANSTO) [17]. The stresses were evaluated from the measured strains in the two principle directions, the in-plane and normal, assuming a bi-axial stress state that has been demonstrated for similar coating systems [18].

The neutron wavelength was selected according to the material, Fe substrate or WC coating, to provide a 90° geometry for the best localization of the gauge volume. Since the thickness of Fe substrates is 3 mm, a high spatial resolution of 0.3 mm was required for this experiment to resolve stress distribution in the through-thickness dimensions. Due to the possibility of using a match-stick gauge volume for the planar sample geometry, the overall gauge volume of $0.3 \times 0.3 \times 20$ mm^3 was sufficient for fast (10 min per point) and accurate (50 μstrain) measurements of the stress profile in the Fe substrates in steps of 0.3 mm. A smaller gauge volume size, $0.2 \times 0.2 \times 20$ mm^3, was used for average through-thickness stress measurements in the coatings, since scanning through 0.3 mm thickness is not required and it was sufficiently small to avoid largely the partial illumination. The zero plane stress conditions were used to address the d_0 problem and its possible variation and to enable the stress calculations without direct measurements of d_0. This method was confirmed in previous experiments on similar coatings [19]. Since, both the Fe substrate and WC phase were measured, this technique

enabled the measurement quality to be independently checked through the stress balance condition.

2.4. Sliding wear behaviour

Wear testing was performed on the flat coating disks using a pin-on-disk tribometer (Microtest, S.A., Spain) with a 6 mm diameter Al_2O_3 ball as the counter body. The coating top surface was polished to 1200 grit and cleaned with ethanol prior to wear testing. The room temperature (RT) wear test was conducted at 10 N load. The sliding distance was 1000 m at a speed of 0.1 m/s with a 10 mm wear-track diameter. The test was repeated three times to assess repeatability. The volume loss of the coating was estimated using laser confocal microscopy (LEXT OLS5000, Olympus, Japan) followed by volume loss analysis through the Lext software (Olympus, Japan). Wear track surface and wear debris were further analysed using SEM and energy dispersive spectroscopy (EDS).

3. Results and discussion

3.1. Coating characterization

Fig. 1 shows that the KM™ technique is capable of achieving WC-Co coatings greater than 300 μm thickness under operating conditions of low gas pressure and temperature. The coating was intact and spallation free at the coating-substrate interface. Porosity measurement using image analysis revealed less than 2% porosity in all the coatings as well as an absence of large voids or a microcrack network. More importantly, etched optical microscopy images in Fig. 1 confirmed plastic deformation (shown by red arrows) and coating particle penetration (shown by yellow arrows) at the interface due to high kinetic energy involvement

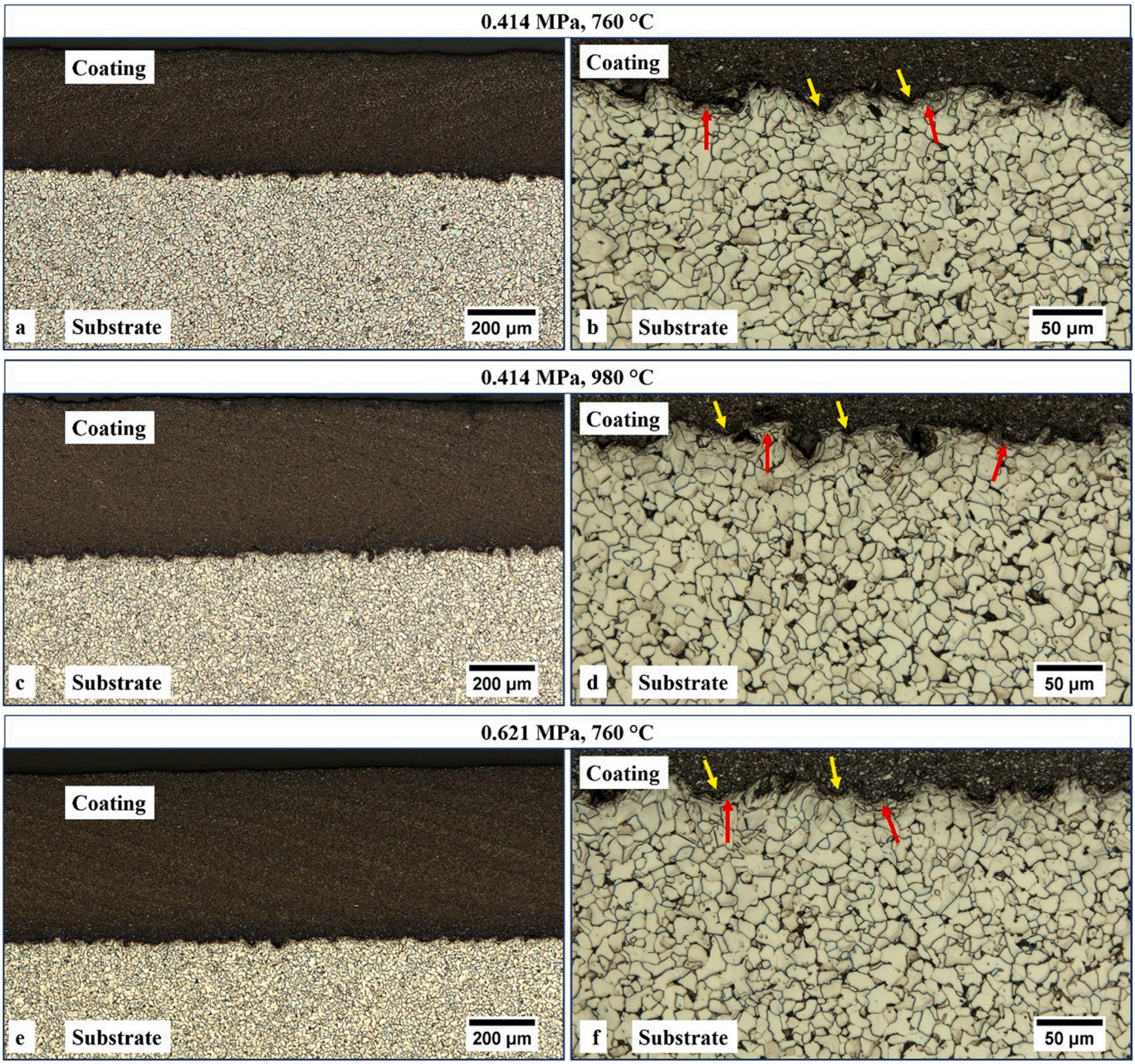

Fig. 1. Etched optical microscopy images of KM™ WC-Co coatings showing uniformity and a clean substrate-coating bond line is shown through micrographs of (a) to (f). Plastic deformation and coating particle penetration into coating surface is shown by red and yellow arrows, respectively. Note the following experimental equivalent units: (i) 0.414 MPa and 760 °C (60 psi and 1400 °F), (ii) 0.414 MPa and 980 °C (60 psi and 1800 °F), and (iii) 0.621 MPa and 760 °C (90 psi and 1400 °F).

in the KM™ system.

The angular grain structure of WC phase observed at high magnification SEM imaging was attributed to retention of WC grains, Fig. 2. This demonstrated an absence of high temperature transformation or the mass dissolution of WC with Co; which is a commonly observed phenomenon in plasma sprayed and HVOF WC-Co coatings [20,21]. Matthews et al. [21] sprayed WC-17wt%Co powder using both HVOF and plasma spraying and indicated significant variation in carbide

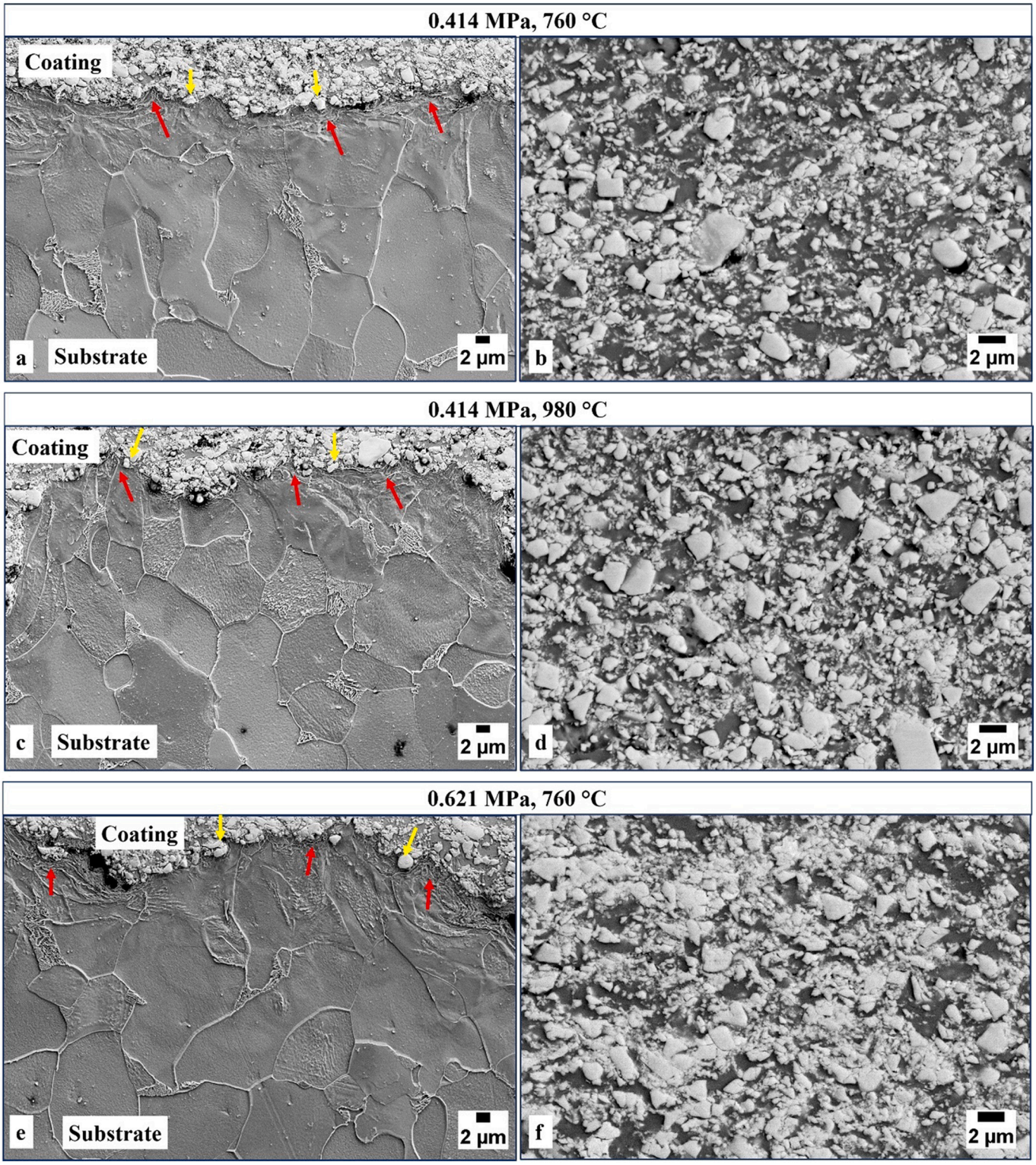

Fig. 2. SEM images of KM™ WC-Co coatings deposited at various spray parameters. Image (a), (c) and (e) shows the plastically deformed zones (red arrows) and particle penetration into the substrate (yellow arrows). Submicron and nano WC particles (grey colour) can be observed through image (b), (d) and (f); surrounding the particles is Co matrix (black colour). Mean free binder path is closest for 90 psi, 1400 °F deposition condition as evidence by image (f). Note the following experimental equivalent units: (i) 0.414 MPa and 760 °C (60 psi and 1400 °F), (ii) 0.414 MPa and 980 °C (60 psi and 1800 °F), and (iii) 0.621 MPa and 760 °C (90 psi and 1400 °F).

dissolution within binder material and decomposition of WC phase. Due to carbide dissolution, WC content was steeply decreased from 85.5 wt% in powder to 21.7 wt% in HVOF and 9.8 wt% in plasma sprayed coating, respectively. In addition, peaks of W_2C, elemental W, WC_{1-x} and Co_6W_6C were also observed in XRD patterns of both type of coatings. Furthermore, the SEM analysis also indicated WC grain fracture. This fracture is associated with the high kinetic energy of the particles during impact against the substrate and subsequent inter-particle collisions that cause large WC particles to fracture and become redistributed within the coating microstructure. The occurrence of matrix phase grain refinement in a composite coating due to grain fracture has been reported previously [1,22] and leads to the increase in the fracture strength of the coating due to the Hall-Petch effect [23,24]. The corresponding microhardness will increase with formation of smaller grains.

The effect of an increase in accelerant gas pressure produced a reduction in the mean free path of the binder. For instance, the 0.621 MPa-760 °C WC-Co coating exhibited a lower binder mean free path, see Fig. 2(f). In addition, an increase in hardness as well as the elastic modulus was observed, see Table 1. The microhardness data revealed that the 0.621 MPa and 760 °C (90 psi and 1400 °F) WC-Co coating exhibited a hardness of 9.6 ± 0.5 GPa (or 970 HV0.3) and elastic modulus of 269.1 ± 3.1 GPa, which were the highest values among all the coatings.

The coating-substrate interface as seen in Fig. 2(a), (c) and (e) exhibited plastic deformation (represented by red arrows) and particle penetration zones (represented by yellow arrows) due to high energy collision of particles onto the substrate. The possible mechanism might include creation of localized plastic region (substrate side) due to high energy particle bombardment leading to grain fracture at the interface (substrate side). In addition, high energy impact might also have generated a rapid localized rise in the temperature at the interface, weakening the substrate, which then triggers particle infiltration into the substrate. Chaudhuri et al. [25] reported similar phenomenon at the interface during cold spraying of Inconel 625 super alloy onto a steel substrate and confirmed the fine layer of grain refinement. Dosta et al. [26] also studied the impact of cold-sprayed WC-Co particles onto Al and Steel substrates and described a similar pattern at the interface. However, in this current work, analysis of the etched optical microscopy images (Fig. 1) and SEM images (Fig. 2), did not observe signs of grain refinement, even at a shallow depth from interface. The substrate consisting of relatively equal sized coarse grains can be observed in Figs. 1 and 2. Only localized plastic regions and particle penetrations were spotted at the interface. It can be cautioned that grain refinement phenomenon can vary according to the specific spray system, input parameters and substrate materials.

The KM™ process does not approach any temperature regime that can cause melting and re-solidification of the WC or Co components. The XRD pattern does not index any W_2C or oxide peaks, while a minor peak of W was observed in all coatings as shown in Fig. 3. Hence, the quenching stresses for a KM™ WC-Co coating should be zero. Moreover, the XRD patterns for various KM™ WC-Co coatings were identical and no peak changes or newly formed peaks were found, Fig. 3. Quantitative Rietveld analysis revealed that there was a minor change in the carbide and Co content at the various temperature and pressure settings of the KM™ process that were explored. Also, the elemental W percentage was minor with respect to the WC and Co weight percentage, which suggests negligible de-carburization, Fig. 3.

Table 1
Microhardness and elastic modulus of KM™ coatings deposited at various parameters.

KM™ WC-Co coatings	Microhardness (GPa)	Reduced modulus, E_r (GPa)
0.414 MPa and 760 °C (60 psi, 1400 °F)	7.6 ± 0.3	174.4 ± 2.9
0.414 MPa and 980 °C (60 psi, 1800 °F)	8.1 ± 0.4	142.8 ± 4.9
0.621 MPa and 760 °C (90 psi, 1400 °F)	9.6 ± 0.5	269.1 ± 3.1

3.2. Microhardness analysis

The 0.621 MPa and 760 °C (90 psi-1400 °F) WC-Co coating exhibited the highest hardness and elastic modulus of the three coatings, Table 1. This high hardness is attributed to its lower mean free binder path and dense coating microstructure, Fig. 2. Thus, pressure increase from 0.414 to 0.621 MPa at 760 °C (60 to 90 psi at 1400 °F) induces a positive effect on mechanical properties of KM™ coatings. However, an increase in the gas temperature to 980 °C (1800 °F) from 760 °C (1400 °F) at constant pressure 0.414 MPa (60 psi), demonstrated an increase in hardness and a reduction in elastic modulus to 143 GPa, Table 1. An explanation to this atypical inverse relationship is related to the size of the Vickers indenter. Microindentation at a load of 3 N would cover a macroscopic volume including both the WC and Co phases, porosity and other microstructural artefacts. Since all the coatings have less than 2% porosity, it is highly unlikely that pores would drastically affect the hardness and elastic modulus value due to their low volume, especially with common indentation practice of indenting in dense area of coatings; a practice that should be discouraged since the results do not reflect the bulk material properties. Also, elastic modulus is a material property and incorporates compliance from indenter as well. Thus, if the indentation occurred on a phase specific, the standard deviation would have been very high due to specific indentation on WC and Co phase, respectively. However, low standard deviation of elastic modulus indicates that the occurrence of phases beneath the indented area is considerably homogenous. In addition, the hard phase WC grain fracture occurred due to the high kinetic energy of the particles during impact against the substrate and subsequent inter-particle collisions. This attributes to fragmentation of large WC particles and their redistribution within the coating microstructures, lowering down the mean free path of binder and improves the mechanical properties of the coatings.

Another hypothesis is that the microhardness values are influenced by residual stresses that are superimposed on the applied indentation stress field within the measurement volume [27]. Residual stresses exert a significant influence on the deformation behaviour around the indent on the coating surface. Therefore, dislocation pile-up may occur under compressive stress, which leads to inconsistencies in the actual contact area of the indenter to the one calculated by the Oliver–Pharr method.

3.3. Macro-stress profiling

Rietveld analysis of coating XRD patterns (Fig. 3) demonstrated that the weight fraction of cobalt (32–35 wt%) was much higher than conventional WC-Co coatings produced by HVOF with cobalt fraction s of 8–15 wt% [28]. The coating material should be considered as a composite and the stress analysis entails both macro and micro-stress aspects. The procedure for discriminating these two stresses can be found elsewhere [29] and only a short description is provided here.

Macro-stress, σ^M, is the long-range stress in the material that is approximated to be homogeneous. Macro-stress is also termed as the "engineering" or "mechanical" stress and assumes that micromechanical distributions of strain/stress fields are averaged through the rule-of-mixture principle into averaged quantities. Macro-stress usually originates from differential plastic deformation or/and thermal history of the different regions of a body. Micro-stress, σ_i^μ, in contrast, is relatively short-ranged to the scale of the sample and varies with respect to the material grain size. Micro-stresses, σ_i^μ where i is the phase index, are typical for multi-phase or composite materials and arise due to the different elastic, plastic, and/or thermal properties of the phases. In any large volume, the micro-stresses are averaged over all phases and balanced to zero according to the rule-of-mixtures.

In principle, macro-stresses can be determined by using diffraction

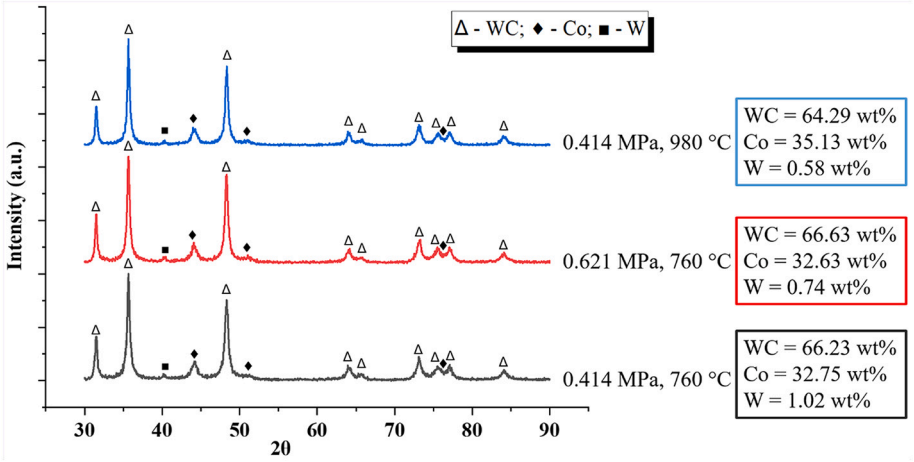

Fig. 3. Indexed XRD spectra of WC-Co coating deposited at various gas pressure and temperature settings in KM™ system along with corresponding phase weight fractions calculated using quantitative Rietveld analysis.

methods for total stresses in all phases and applying the rule-of-mixtures. This assumes that the stress-free (or d_0) lattice parameters are available to calculate the total phase stresses. Specifically, for coatings, there are two conditions that help for the stress analysis: (i) the stress state is biaxial with two principal directions (in-plane and normal, or || and ⊥) and (ii) the condition $\sigma^M = 0$ is valid with great accuracy, especially for thin coatings. Even when the stress-free lattice parameters are not known, the strain-stress equations can be resolved to derive the macro-stress [30].

In this study, the stress-free lattice spacing (d_0) for WC phase was known. However, it was not possible to measure the cobalt phase due to the specific neutron scattering properties of cobalt that makes such measurements impractical. In these circumstances, the macro-stress in the coating, formally speaking, could not be evaluated directly through weighted averaging of the two phases. However, the macro-stress in the coating was possible to evaluate indirectly using the stress balance between total stress in the substrate and the coating, which equilibrates to zero. As shown by Luzin et al. [30], the macro-stress in the coating and stress measured in one phase of the composite coating can be split as the deviatoric part of the micro-stress tensor. In the case of this work macro-stress is determined indirectly through the balance condition and, as well, stress can be measured in the WC phase. This split in stress was detected and statistically treated as the presence of the deviatoric part of the micro-stress, which is evidence of microstructural anisotropy.

Fig. 4 shows a typical through thickness residual macro-stress profile of the KM™ WC-Co coatings, where the experimental points are shown as symbols. In accordance with the general principles defined above, the measurements in the substrate represent the true macro-stress, while measurements in the composite coating can have a contribution from the deviatoric stress micro-stress component as well as the macro-stress component.

The final residual stress distribution is a complex superposition of stresses generated within the coating and substrate system. The disintegration of the stress profile into different contributions is the basis of the quantitative analysis of the experimental data. To achieve this goal, the distributions of macro-stress were further analysed, attributing the stress state to several contributions under the formalism of the Tsui & Clyne [31].

3.4. Contributors to the residual stress

In our model approach, the following contributions were considered: (i) Thermal contraction stresses due to the mismatch between the coefficients of thermal expansion (CTE) between the substrate and coating, in the presence of the temperature drop from the end-of-spray to room

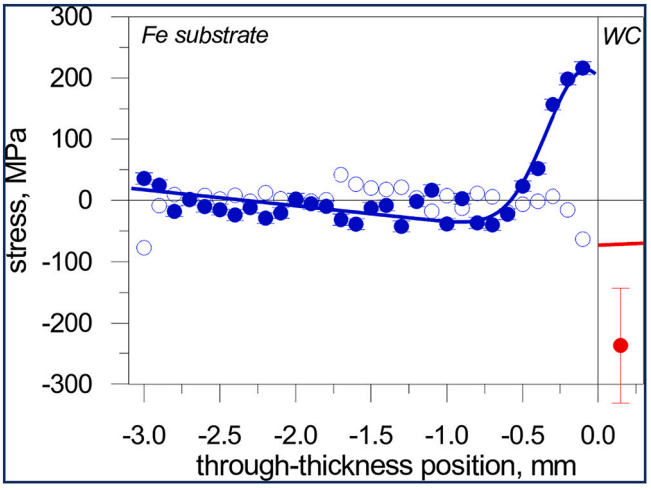

Fig. 4. Through thickness residual stress profile scan results of WC-Co coating deposited at 0.414 MPa and 760 °C (60 psi and 1400 °F). The solid circle symbols represent experimental points and the lines correspond to the model calculations from fitting the experimental results. The blank circle symbols correspond to the stress profile after grit-blasting.

temperature, (ii) deposition (or, for KM™, 'peening') stress from the bombardment of high speed WC-Co particles, and (iii) self-equilibrating stress in the substrate that was generated prior to the coating deposition. The sources of stress within the coating and substrate superimpose to establish the residual stress state of the coating/substrate system. However, with a single point measured in the coating, it is difficult to fit the experimental data with a model profile unambiguously. Therefore, several parameters were experimentally determined and used as fixed parameters for quantitative data analysis, see Table 2 for details.

The three contributions mentioned above, under quantitative considerations, can be characterized. In particular, (i) ΔCTE between the coating and substrate materials and the temperature drop after the spray process, ΔT, can be obtained from measurements. The thermal expansion difference, Δα, is determined from $\Delta\alpha = \alpha_{coat} - \alpha_{sub}$, where α_{coat} can be accurately evaluated on the basis of the volume fractions of cobalt and WC; while α_{sub} is known from standard material property measurements. Second, (ii) the deposition stress was set to a value of zero since the peening effect generates compressive stress, which are typical for the cold spray materials. The peening stresses are approximately equilibrated by the quenching effects that generate tensile stress.

Table 2
Summary of residual macro-stress analysis. Note the following experimental equivalent units: (i) 0.414 MPa and 760 °C (60 psi and 1400 °F), (ii) 0.414 MPa and 980 °C (60 psi and 1800 °F), and (iii) 0.621 MPa and 760 °C (90 psi and 1400 °F).

Spray conditions: gas pressure/temperature	Measured deposition temperature of substrate (°C)	Differential thermal coefficient $\Delta\varepsilon = \Delta\alpha\Delta T$ (μstrain)	Thermally generated stress in coating (MPa)	Deposition stress (MPa)	Total residual stress (MPa)
0.414 MPa, 760 °C (60 psi, 1400 °F)	150 ± 20	−410 ± 50	−71 ± 7	0	−71 ± 7
0.414 MPa, 980 °C (60 psi, 1800 °F)	200 ± 20	−570 ± 60	−80 ± 8	0	−80 ± 8
0.621 MPa, 760 °C (90 psi, 1400 °F)	100 ± 20	−250 ± 50	−59 ± 11	0	−59 ± 11

Since, the given spraying regime combines features of two effects opposite in terms of the residual stress generation (high peening action and high energy input), the expected value of the deposition stress can really be close to zero. If not perfect zero, then the further analysis can be biased by the small value of the deposition stress since any non-zero deposition stress in thin coatings (thickness of coating is much less than the thickness of the substrate) results in almost constant residual stress of the same value (for thick coatings the deposition stress and residual stress might differ greatly). This possibility will be discussed in detail later. Also, the uncertainty of the deposition stress in this case, some 100 MPa, does not allow accurate analysis of this parameter, since typical values of the deposition stress is in the range of ±100 MPa [32], though even with these error bars some general trend can be traced out.

Finally, (iii) the third contribution is the self-balanced stress in the substrate that demonstrated the sharp gradient in the interface region with tensile stress peaking up to ~300 MPa. In general, the spray process is associated with compressive zone in the near-to-interface region of the substrate due to peening effects from the grit blasting or peening effect of the sprayed hard particles to ~0.5 mm depth in the substrate [33,34]. However, in the current study, the measured stress profile demonstrates an opposite footprint with a tensile zone, which is associated with the thermal impact on the substrate surface. This profile, however, can be quantitatively described by a Gaussian-like distribution by three parameters: the amplitude, the centre position and the width parameter. The three shape parameters were used to fit the experimental profiles.

The superposition of the above three contributions results in the distribution shown in Fig. 4 as an experimental profile (solid circle data points) and a model profile (solid lines), which are in a good quantitative agreement with a chi-square per degree of freedom of less than 5. In the same figure, the stress profile after grit-blasting is also plotted to demonstrate slightly compressive stress near the surfaces of the substrate that is typical for this kind of substrate surface treatment before spraying.

3.5. Overall stress profiling

The residual macro-stress measurements for the steel substrate and WC-Co coating revealed that compressive stresses developed in the coatings. The magnitude of compressive stress in the WC-Co coatings were around 100 MPa, see Table 2. Such compressive stresses in the coatings are mainly due to the large difference in CTE between the coating and substrate materials [35–37]. Therefore, thermal contraction stresses arise due to the large ΔCTE as well as localized substrate heating from the high kinetic energy impacted particles. These thermal stresses dominated the deposition or peening stresses; which can be neglected relative to the thermal mismatch stress. Subsequently, for the overall coating, stresses are compressive and thermally generated in nature.

It can be mentioned that the absolute value of the macro-stress, ~100 MPa (compressive), is significantly lower than previously reported in similar WC-Co or WC-Ni coatings, though deposited by HVOF. A more typical value of macro-stress in WC-Co coatings made by HVOF is rather 500 MPa (compressive), e.g. [30]. Two obvious reasons for that effective decrease of the residual stress in cold spray are (i) higher spraying temperatures used in HVOF inducing larger thermally generating stresses and (ii) larger volume fraction of the metal binder in the composite coating that effectively play a role of stress relaxation phase. In fact, the residual stress in pure Co coatings deposited by cold spray tends to be negligible [29]. Thus, this is not surprising that the observed residual stress in cold spray coating fall in the range from zero stress, typical for pure Co cold spray, to ~500 MPa in HVOF WC-richer coatings.

Although the thermal mismatch stress dominates the experimentally observed stress profiles, the other two contributions can also be discussed. Whereas the method of surface preparation should not have introduced any tensile stress since grit or sand blasting usually generates a zone of compressive stress under the interface [28], the experimental results assume an alternative interpretation, Fig. 4. Tensile stresses that are observed at the substrate interface usually arise from laser and thermal treatments or machining operations. There was no machining carried out prior to spraying these samples, hence it could be inductively gathered that there was localized heat generated in the KM™ process that was similar to a laser or thermal surface treatment. This localized heat is speculated as modifying the stress state of the substrate, which requires further investigation.

The evaluation of the total stress follows summation of both macro and micro-stresses. The macro-stress was already estimated above. The micro-stress can also be derived since total stress = macro-stress + micro-stress. The results of this evaluation, Table 3, are provided as two ways of the tensor representation; (i) through the hydrostatic H^{μ} and deviatoric D^{μ} parts, and (ii) through $\sigma^{\mu}_{11} = \sigma^{\mu}_{22}$ and σ^{μ}_{33} micro-stress tensor components. The micro-stresses are presented only for the WC phase, since stress in the Co matrix balances the average micro-stress to exactly zero. The results of the micro-stress analysis is that, (i) the micro-stress state is anisotropic with the in-plane and normal directions being different, (ii) the micro-stress is compressive for the WC and tensile for Co, (iii) the magnitude of the in-plane micro-stress is relatively small,

Table 3
Summary of residual micro-stress analysis of WC phase. Note the following experimental equivalent units: (i) 0.414 MPa and 760 °C (60 psi and 1400 °F), (ii) 0.414 MPa and 980 °C (60 psi and 1800 °F), and (iii) 0.621 MPa and 760 °C (90 psi and 1400 °F).

Spray conditions: gas pressure/temperature	Measured temperature on the back (°C)	Hydrostatic part H^{μ} of micro-stress (MPa)	Deviatoric part D^{μ} of micro-stress (MPa)	In-plane σ^{μ}_{11} micro-stress (MPa)	Normal σ^{μ}_{33} micro-stress (MPa)
0.414 MPa, 760 °C (60 psi, 1400 °F)	150	−30	−66	−195	2
0.414 MPa, 980 °C (60 psi, 1800 °F)	200	−203	−39	−242	−125
0.621 MPa, 760 °C (90 psi, 1400 °F)	100	−88	−48	−135	8

less than −200 MPa, and (iv) the micro-stress depends on the spray conditions.

To explore the interpretation of the observed micro-stresses, a model approach employed the Hashin-Strikman (HS) method to evaluate the upper and lower stress bounds. The major focus was on evaluating the thermally generated stress due to significant ΔCTE of the two components of the composite coating: $\alpha_{WC} = 5.2 \times 10^{-6}\ 1/K$ and $\alpha_{Co} = 13.8 \times 10^{-6}\ 1/K$. In addition, other composite coatings of a dual phase steel formed by cold spray have demonstrated the thermal mechanism for micro-stress formation [34].

The results of the thermally generated micro-stress calculation are given in Fig. 5, which shows that the micro-stress can be interpreted in terms of the thermal mechanism. Hence the sign and magnitude of the micro-stress can be supported; especially the σ^{μ}_{11} component that fits the calculated bounds. The experimental fact that σ^{μ}_{11} and σ^{μ}_{33} are different arises through microcracking that is preferably oriented parallel to the surface. Such microcracking causes micro-stress relaxation in the normal direction. The anisotropic micro-stress effect is much less pronounced in the sample sprayed at the highest temperature with $\sigma^{\mu}_{11} \sim \sigma^{\mu}_{33}$, while for the lower sprayed temperatures $\sigma^{\mu}_{33} \sim 0$. This result agrees with the notion that a higher temperature provides better particle adhesion with less microcracking. This is corroborated by the fact that the elastic modulus of the sample sprayed at high temperatures (~270 GPa at 0.414 MPa and 980 °C (60 psi and 1800 °F)) is higher than corresponding samples sprayed at lower temperatures (~150 GPa at 0.414 MPa and 760 °C (60 psi and 1400 °F)) since the elastic modulus is also sensitive to particle adhesion.

Although these observations present a non-contradictory picture of the micro-stress nature, the large experimental error bars prevent more accurate analysis. For example, there might be an additional effect related to the differential plastic deformation. Thus, Co can plastically deform, while WC is non-deformable, but this effect should be even less in its magnitude than the thermally generated stress. Therefore, such an effect cannot be quantitatively considered with the given experimental uncertainties.

3.6. Modelling of the micro-stress

The stress relaxation of the σ^{μ}_{33} component can be assessed through modelling; Fig. 6. The condition of $\sigma^{\mu}_{33} = 0$ is imposed; i.e., assuming the relaxation in the normal direction, while the thermally generated stresses are calculated under the same conditions for the bulk composite discussed above. The numerical data are provided in Table 4. The experimental results and the calculated values are in good correlation even though the temperature drop parameters were not adjusted but taken as the experimentally estimated values. However, good agreement is achieved without any adjustment and confirms of the assumption about oriented microcracking. The effective temperature was underevaluated since there is inconsistency of the hydrostatic part (Fig. 6 (b)), which is not surprising since the temperature was measured from the back side of the substrate while the actual temperature of the composite formation could be higher.

The outcomes of the stress analysis allow a test for the deposition stress assumption being equal to zero. There is a correlation of the macro- and micro-stress values extracted from the experimental result. Thus, assuming any other value of the deposition stress, shifts the values of the micro-stress. Specifically, if deposition stress is set to 100 MPa, then the σ^{μ}_{33} value shifts to positive 175 MPa. This is impossible for the assumption of the thermally generated stress mechanism, which can be either negative or zero in case of full stress relaxation due to the microcracking. Thus, the micro-stress analysis confirms that if the deposition stress is non-zero, then the deposition stress could only be negative (i.e., compressive). However, the negative deposition stress, cannot be of large magnitude; otherwise the balance between σ^{μ}_{11} and σ^{μ}_{33} shifts to the opposite situation and this is unlikely.

The results of the microstructural, mechanical and residual stress characterization allow the major coating formation concepts to be schematically presented in Fig. 7. The microstructural observations suggest that feedstock particles attained high kinetic energy due to a combination of heavy WC particles and the KM™ system's velocity gas stream. These high energy WC particles impact the substrate and result in considerable plastic deformation to the substrate and particle penetration. High kinetic energy associated with the particle breaks down the large substrate grains to smaller grains, leading to localized grain refinement to a limited depth. While the WC particles undergo brittle fracture, the Co particles are ductile and experience plastic deformation. The deformation of Co metal binds these WC grains but are chemically inactive.

The residual macro- and micro-stress analysis brings more details of the thermo-mechanical interactions into this picture. The initial large amount of friction dissipation and localized heating due to high energy impact on the steel substrate surface lead to tensile stresses in the subsurface region under the substrate-coating interface. A combination of nearly balanced peening and quenching effects in the coating material leads to overall deposition stresses close to zero. The dominating thermal contraction due to differences in CTE of the coating and substrate

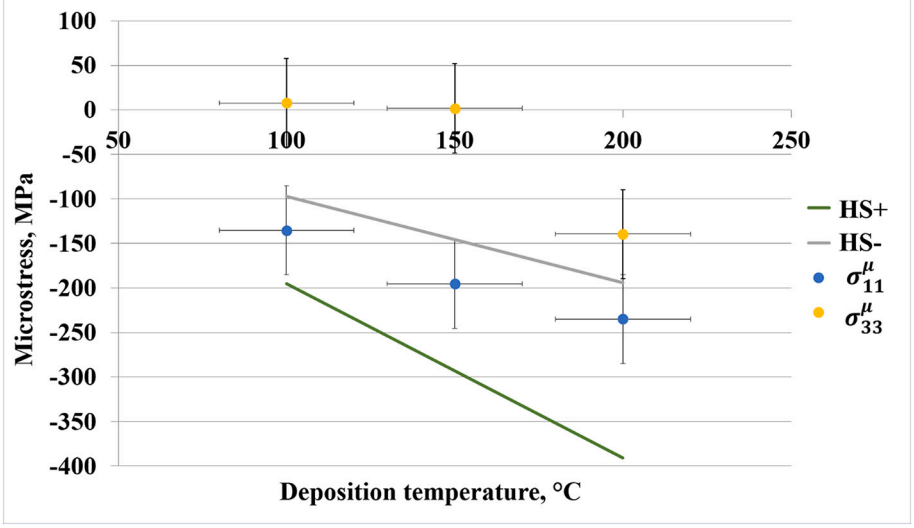

Fig. 5. The experimental WC micro-stress data (symbols) against theoretically predicted micro-stress due to the thermal mismatch between WC and Co.

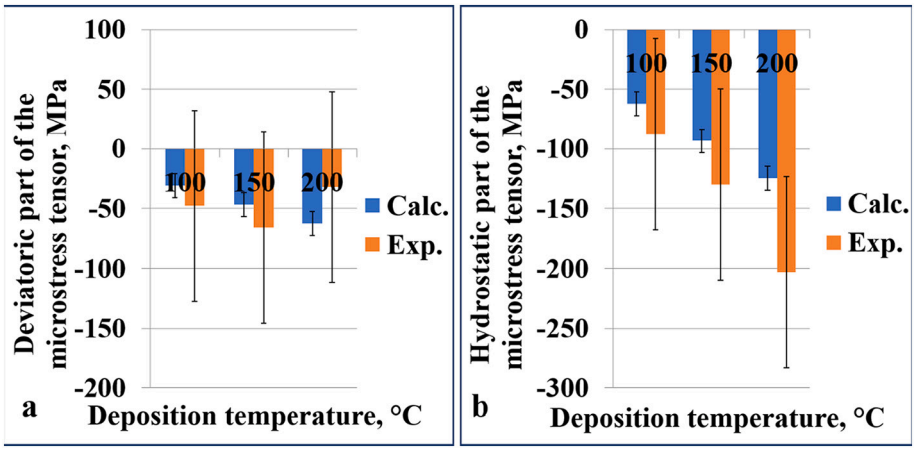

Fig. 6. Comparison of the experimental result vs. modelling by means of (a) deviatoric part and (b) hydrostatic part of the micro-stress tensor for the WC phase. The error bars of the calculated values are due to measured temperature uncertainty propagated to the stress values.

Table 4
Summary of the HS-residual micro-stress theoretical evaluation. Note the following experimental equivalent units: (i) 0.414 MPa and 760 °C (60 psi and 1400 °F), (ii) 0.414 MPa and 980 °C (60 psi and 1800 °F), and (iii) 0.621 MPa and 760 °C (90 psi and 1400 °F).

Spray conditions: gas pressure/ temperature	Accepted temperature drop (°C)	Calculated hydrostatic micro-stress (MPa)	Calculated hydrostatic part of micro-stress when $\sigma_{33} = 0$ (MPa)	Calculated deviatoric part of micro-stress when $\sigma_{33} = 0$ (MPa)
0.414 MPa, 760 °C (60 psi, 1400 °F)	150	−140	−47	−93
0.414 MPa, 980 °C (60 psi, 1800 °F)	200	−187	−62	−125
0.621 MPa, 760 °C (90 psi, 1400 °F)	100	−93	−31	−62

materials leads to compressive macro-stresses in the coating. However, it is noted that attributing the large magnitude of compressive stress to thermal contraction over the deposition stress is difficult to quantify because of the relatively large error bars of 100 MPa. The limited uncertainty is associated with the difficulties of strain measurement of the elastically hard materials, such as WC with elastic modulus of 680 MPa. These materials require high resolution compatible to (i) the coating thickness of 0.3 mm, (ii) 50 vol% of Co binder and, (iii) high background from Co incoherent scattering.

Microscopically, the mechanism of micro-stress formation is explained through complex interactions between the ductile Co, brittle WC particles with fracture and thermal mismatch between composite phases, WC and Co; where all mechanisms occur under conditions of a temperature drop after coating deposition.

3.7. Sliding wear behaviour

In general, WC-Co based composite coatings are recognized for their wear resistant capabilities against sliding, erosion and abrasion wear at room temperatures and up to 500 °C [38]. Hence, the room temperature sliding wear behaviour of current KM™ WC-Co coatings were also analysed using the pin-on-disk method against Al_2O_3 as the counter body. Table 5 summarizes the volume wear rate obtained for the KM™ WC-Co coatings and compares these wear results with WC-Co based coatings manufactured using either HVOF, cold spray or an electrolytic hard chrome process.

Table 5 shows that KM™ WC-Co coatings, even with relatively low WC content, exhibited equivalent wear resistance to both HVOF and cold sprayed WC-Co coatings that have a high WC content. The KM™ process is advantageous for coating WC-Co powders with desirable mechanical properties due to the absence of decarburization and decomposition, as evidenced by their XRD pattern shown in Fig. 3.

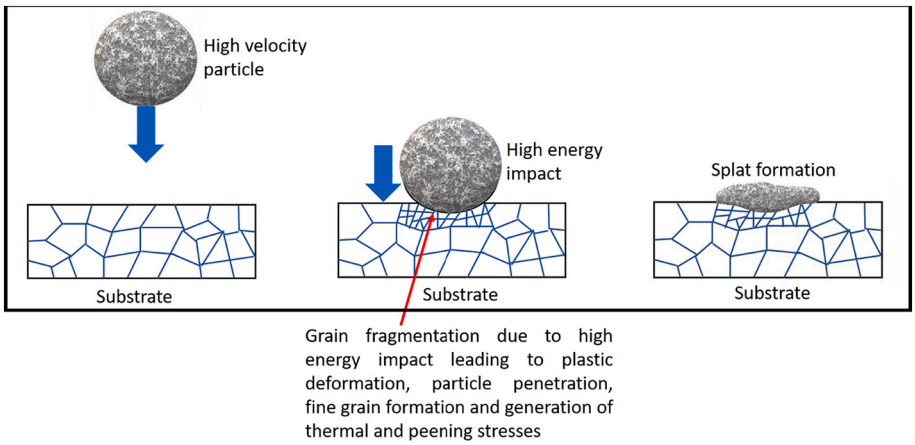

Fig. 7. A summary of KM™ processing of WC-Co coatings and the resulting microstructure.

Table 5
Summary of volume wear rate of KM™ WC-Co coatings and their approximate comparison with conventionally sprayed WC-Co coatings and electrolytic hard chrome coating. Note the following experimental equivalent units: (i) 0.414 MPa and 760 °C (60 psi and 1400 °F), (ii) 0.414 MPa and 980 °C (60 psi and 1800 °F), and (iii) 0.621 MPa and 760 °C (90 psi and 1400 °F).

Composition	Manufacturing process	Abrasion media	Applied load	Wear speed	Wear distance	Volume wear rate	Reference
WC-Co	KM™ (0.414 MPa and 760 °C)	Al_2O_3	10 N	0.1 m/s	1000 m	9×10^{-7} mm^3/N-m	Current study
WC-Co	KM™ (0.414 MPa and 980 °C)	Al_2O_3	10 N	0.1 m/s	1000 m	18×10^{-7} mm^3/N-m	Current study
WC-Co	KM™ (0.621 MPa and 760 °C)	Al_2O_3	10 N	0.1 m/s	1000 m	6×10^{-7} mm^3/N-m	Current study
WC-17Co	CS	–	10 N	0.6 m/s	–	5.56×10^{-6} mm^3/N-m	[39]
WC-12Co	CS	WC-12Co	25 N	~0.2 m/s	1000 m	$\sim 1.6 \times 10^{-7}$ mm^3/N-m	[10]
WC-17Co	CS	WC-12Co	25 N	~0.2 m/s	1000 m	$\sim 3.6 \times 10^{-7}$ mm^3/N-m	[10]
WC-25Co	CS	WC-12Co	25 N	~0.2 m/s	1000 m	$\sim 4.4 \times 10^{-7}$ mm^3/N-m	[40]
WC-25Co	CS	WC-12Co	25 N	~0.2 m/s	1000 m	$\sim 4 \times 10^{-7}$ mm^3/N-m	[41]
WC-12Co	HVOF	Al_2O_3	107 N	0.2 m/s	1000 m	$2.5 \pm 0.7 \times 10^{-6}$ mm^3/N-m	[42]
WC-17Co	HVOF	Diamond	60 N	0.03 m/s	20 m	$\sim 1.2 \times 10^{-4}$ mm^3/N-m	[43]
WC-25Co	HVOF	WC-12Co	25 N	~0.2 m/s	1000 m	$\sim 2 \times 10^{-6}$ mm^3/N-m	[41]
WC-12Co	HVOF	WC-12Co	25 N	~0.2 m/s	1000 m	$\sim 3.7 \times 10^{-7}$ mm^3/N-m	[11]
WC-17Co	HVOF	WC-12Co	25 N	~0.2 m/s	1000 m	$\sim 1.2 \times 10^{-6}$ mm^3/N-m	[11]
WC-12Co	HVOF	–	7 N	~0.02 m/s	60 m	$4.74 \pm 0.28 \times 10^{-6}$ mm^3/N-m	[44]
WC-10Co-4Cr	HVOF	WC-6Co	30 N	0.10 m/s	–	3.6×10^{-9} mm^3/N-m	[45]
WC-10Co-Cr	HVOF	WC-6Co	318 N	0.05 m/s	500 m	9.81×10^{-7} mm^3/N-m	[46]
Electrolytic hard chrome coating	–	–	10 N	0.6 m/s	–	2.25×10^{-5} mm^3/N-m	[39]

Decomposition of WC-Co coatings during HVOF spraying is regarded as deleterious in terms of wear resistance since (i) the WC phase decomposes into brittle W_2C phase, and (ii) the ductile binder is replaced by a relatively brittle, amorphous phase [21]. Wear is then characterized by the combined action of a brittle W_2C and a brittle binder phase containing high concentrations of dissolved tungsten, which contributes to inferior coating cohesion [20]. The wear performance of the KM™ WC-Co coatings under the experimental conditions was superior to electrolytic hard chrome plating, even though the KM™ coatings exhibited a low hard phase (WC) content.

In comparison, the 0.621 MPa and 760 °C (90 psi and 1400 °F) WC-Co coating exhibited better wear resistance than the 0.414 MPa and 760 °C (60 psi and 1400 °F) and 0.414 MPa and 980 °C (60 psi and 1800 °F) WC-Co coatings as evidenced by their measured volume wear rate, Table 5. As discussed earlier, the 0.621 MPa and 760 °C (90 psi and 1400 °F) WC-Co coating displayed the highest hardness (9.86 GPa) and lowest binder mean free path (Fig. 2) among the three coatings, which together lead to superior wear resistance. It has been reported that the wear resistance of WC-Co based composite material is proportional to both hardness and binder mean free path [47]. Thus, a lower binder mean free path and high hardness, in combination, enhanced the wear resistance of the 0.621 MPa and 760 °C (90 psi and 1400 °F) WC-Co coating. Regardless, the wear rate values of all coatings were of the order of 1×10^{-7} mm^3/N-m and indicated "mild wear" behaviour.

3.8. Morphology and composition of worn surfaces

The wear tracks of the KM™ WC-Co coatings were evaluated by SEM and EDS to comprehend the wear mechanism; see Fig. 8. Low magnification wear tracks images of all three coatings demonstrated distinct surface characteristics with the common appearance of smooth surface and shallow grooves that indicate a dominant abrasive wear mechanism,

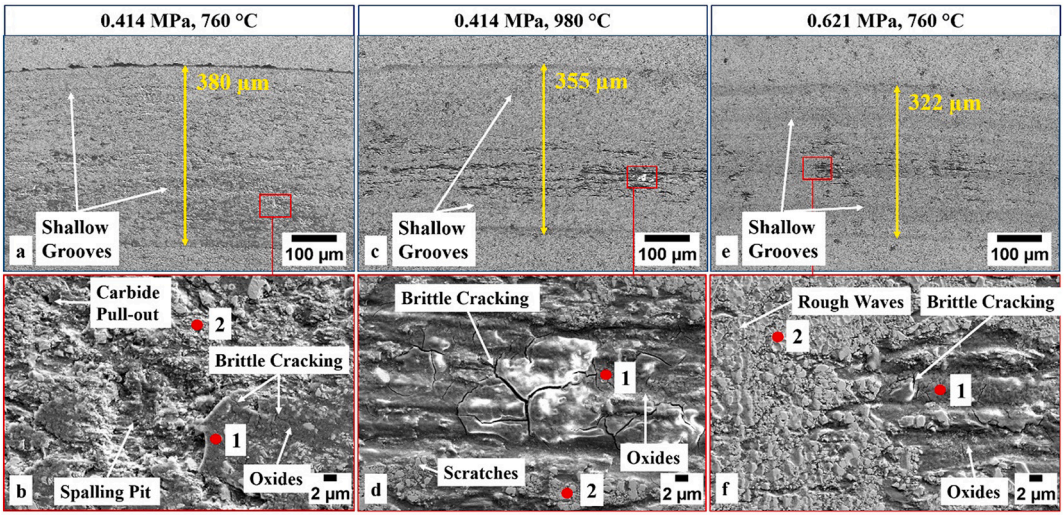

Fig. 8. SEM images of the worn surface of KM™ WC-Co coatings produced with different pressure and temperature settings (a) 0.414 MPa and 760 °C, (c) 0.414 MPa and 980 °C and (e) 0.621 MPa and 760 °C. The corresponding high magnification images of red boxes drawn in (a), (c) and (e) are shown in (b), (d) and (f), respectively. Note the following experimental equivalent units: (i) 0.414 MPa and 760 °C (60 psi and 1400 °F), (ii) 0.414 MPa and 980 °C (60 psi and 1800 °F), and (iii) 0.621 MPa and 760 °C (90 psi and 1400 °F).

Fig. 8. In addition, the sliding wear damage enforced by the Al_2O_3 counter body was concentrated more towards the central region of the wear tracks; as suggested by the dark patches within the three wear tracks. Hence, material loss is not uniform across the wear track, but occurs preferentially in the middle of the wear track at the point of the highest Hertzian pressure.

High magnification SEM images of the 0.414 MPa and 760 °C (60 psi and 1400 °F) WC-Co KM™ coating wear track of width 380 μm revealed carbide pull-out, scratches, brittle cracking and formation of spalling pits due to accumulative detachments of both WC and binder Co phases, Fig. 8(b). In addition, EDS analysis of points 1 and 2 indicated in Fig. 8 (b) disclosed the formation of oxides throughout the wear track. Hence, an oxide film formed due to localized temperature excursions from frictional forces. Subsequently, this soft oxide film acted as a protection film that shields the surface from further damage and, thus, the wear rate is reduced to a relatively steady wear rate.

Intriguingly, EDS analysis at point 1 on dark patches, not only discovered the presence of high oxygen content but also aluminium from the counter body. In addition, the elemental content of both W and C was found to be lower at these points. The appearance of oxygen in the dark patches was a combined effect of frictional temperature rise and material transfer from the counter body. Embedment of aluminium particles within the wear surface attributed to the adhesive wear characteristics. Another important observation was brittle cracking within the dark oxide patches, which induces the detachment of coating material and created the spalling pits as observed in Fig. 8(b). Therefore, the wear of the 0.414 MPa and 760 °C (60 psi and 1400 °F) WC-Co KM™ coating was the accumulative action of abrasive, adhesive and oxidative wear mechanisms.

In contrast, the 0.414 MPa and 980 °C (60 psi and 1800 °F) WC-Co KM™ coating suffered significant coating surface damage as evidenced by a valley of dark patches within the central portion of the wear track of width 355 μm, Fig. 8(c). Moreover, excessive brittle cracking and scratches were visible at high magnification images of the wear track, Fig. 8(d). EDS of points 1 and 2 shown in Fig. 8(d) indicated the development of oxides throughout the worn surface. In addition, point 1 indicated transfer of counter body material to the wear surface, but to a lesser extent than the 0.414 MPa and 760 °C (60 psi and 1400 °F) WC-Co KM™ sample. The presence of continuous wide dark patches with severe brittle cracking is probably the major reason for the high-volume wear rate of this coating compared to the other two coatings. Thus, the wear mechanism was the combination of abrasive, adhesive and oxidative wear mechanisms, as also described for the previous material (i.e., 0.414 MPa and 760 °C (60 psi and 1400 °F) WC-Co KM™ coating).

The wear track of the 0.621 MPa and 760 °C (90 psi and 1400 °F) WC-Co KM™ coating with a width of 322 μm displayed the formation of shallow grooves, rough waves due to plastic deformation, and random dark patches that were concentrated towards the central portion of the sample, Fig. 8(e). The dark patches were small in comparison to the 0.414 MPa and 980 °C (60 psi and 1800 °F) WC-Co KM™ coating worn surface and exhibited very few brittle cracks. The major portion of the worn surface was covered by features described as rough waves and which were attributed to plastic deformation and extrusion of the binder phase with the protrusion of WC grains in a characteristic wave pattern, Fig. 8(f). EDS of points 1 and 2 in Fig. 8(f) also indicated the formation of oxides and transfer of counter body material. The material loss occurred mainly from the dark portions on the worn surface. Thus, the concurrent action of an inhibitive oxide film and W, C and Co rich rough waves lead to the superior wear resistant of the 0.621 MPa and 760 °C (90 psi and 1400 °F) WC-Co KM™ coating compared to the 0.414 MPa and 760 °C (60 psi and 1400 °F) and 0.414 MPa and 980 °C (60 psi and 1800 °F) WC-Co KM™ coatings. However, the operative wear mechanism was similar to the other two coatings; i.e., a combination of abrasive, oxidative and adhesive wear.

Interestingly, width of wear track (380 μm) for 0.414 MPa and 760 °C WC-Co KM™ coating was bigger than 0.414 MPa and 980 °C coating (355 μm), but, displayed lower volume wear rate as compared to former when measured using laser confocal microscopy. This is attributed to the disproportionate removal of coating material from centre portion of the coating as evidenced by SEM images in Fig. 8(a) and (b). SEM images of 0.414 MPa and 980 °C coating with smaller wear track width demonstrated a continuous valley of dark patches with extensive brittle cracking, ascribing to high material loss, Fig. 8(c) and (d). However, SEM images of 0.414 MPa and 760 °C coating, even with bigger worn surface width, shown wear track without severe dark patches and predominantly unveiled a homogenous surface throughout the track, Fig. 8(a) and (b). More importantly, the 0.621 MPa and 760 °C (90 psi and 1400 °F) WC-Co KM™ coating exhibited the lowest volume wear rate due to a combined effect of low mean free binder path and development of both an oxidation layer and a morphology described as rough waves. After the preferential removal of soft binder phase, the waves were composed mainly of protruding WC grains that bear the maximum sliding load. The EDS results, Table 6, indicate that there was no material transfer within these waves due to the absence of adhesive wear; resulting in a low volume wear rate and smooth surface [48].

The combined SEM and EDS analysis of the worn surfaces of individual WC-Co KM™ coatings identify cobalt extrusion and micro-abrasion as the main wear mechanisms. When a hard Al_2O_3 counter body slides against the WC-Co coating, the binder phase composed of ductile Co is removed preferentially and endures severe plastic deformation, Fig. 8. The centre of wear track endures the extreme load of the counter body. Hence, the support for the WC grains from the Co matrix is reduced due to a combination of plastic deformation and micro-abrasion. Subsequently, micro-cracking and carbide pull-out leads to plate-like wear debris that is Co rich, Figs. 9(a) and 10. Moreover, there is a localized temperature rise due to high frictional heat that induces the oxide formation on the worn surface as evidenced by the EDS analysis mentioned in Table 6 and the high oxygen content within the wear debris, Fig. 10(a). The formation of a smooth oxide layer on the coating surface during sliding reduces the material loss. However, repeated sliding of the coating against the counter body cracks the brittle oxide layer and produces fine Co-rich oxide debris developed by extrusion and micro-abrasion, Figs. 8 and 9(a).

Adhesive wear was evident as counter body material transfer within the worn surface; especially within the heavily deformed surface aligned towards the centre portion of the wear track where load-bearing was undertaken by binder phase-based oxides due to removal of WC particles. It is intriguing to notice material transfer from a smooth Al_2O_3 ball to a relatively rough WC-Co KM™ produced coatings. To understand the operating mechanism, surface of Al_2O_3 ball was analysed using optical microscope, which was used as counter body for wear testing the 0.414 MPa and 760 °C coating, Fig. 9(b). The surface of Al_2O_3 ball sustained dark patches with the characteristics same as spalling pits, showcasing the material removal and, revealed extensive wear track marks forming grooves and scratches on worn surface. In addition, cracks are visible on the ball surface attributing to heavy sliding action against hard WC-Co coatings. These cracks probably have formed during recurring gliding

Table 6
EDS results of points 1 and 2 in wear tracks of KM™ WC-Co coatings as shown in Fig. 8. Note the following experimental equivalent units: (i) 0.414 MPa and 760 °C (60 psi and 1400 °F), (ii) 0.414 MPa and 980 °C (60 psi and 1800 °F), and (iii) 0.621 MPa and 760 °C (90 psi and 1400 °F).

KM™ WC-Co coatings	Point	Elemental content (at.%)				
		W	C	Co	O	Al
0.414 MPa, 760 °C (60 psi, 1400 °F)	1	8.37	5.01	14.11	68.02	4.49
	2	42.03	22.10	15.43	20.44	–
0.414 MPa, 980 °C (60 psi, 1800 °F)	1	10.90	3.40	22.40	61.29	2.00
	2	47.34	14.68	24.52	13.46	–
0.621 MPa, 760 °C (90 psi, 1400 °F)	1	8.26	4.18	34.36	52.17	1.03
	2	46.89	35.60	17.52	–	–

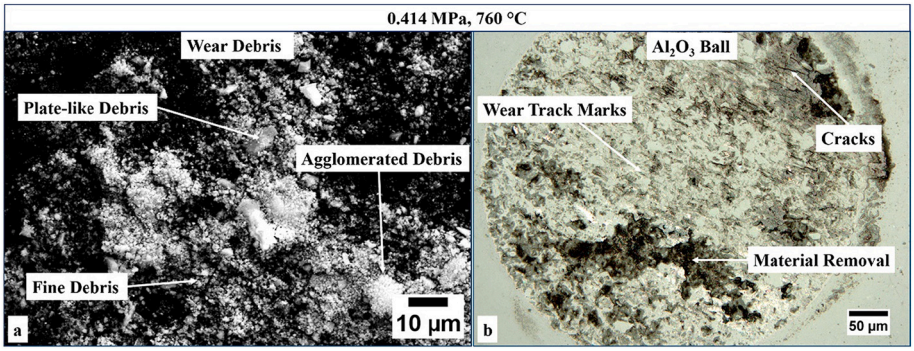

Fig. 9. (a) SEM image of wear debris produced during wear testing and, (b) optical microscope image of Al_2O_3 ball used as counter body for wear testing the 0.414 MPa and 760 °C (60 psi and 1400 °F) KM™ WC-Co coating.

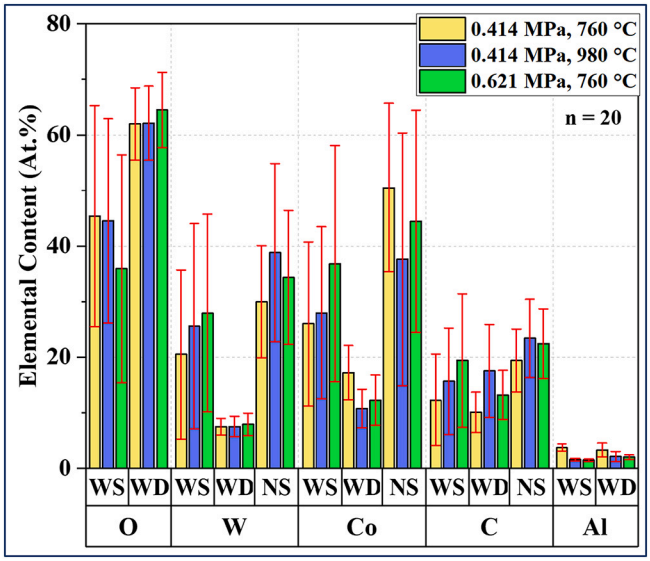

Fig. 10. Comparative EDS analysis of average elemental content of the wear surface (WS), normal surface (NS) and wear debris (WD). Note the following experimental equivalent units: (i) 0.414 MPa and 760 °C (60 psi and 1400 °F), (ii) 0.414 MPa and 980 °C (60 psi and 1800 °F), and (iii) 0.621 MPa and 760 °C (90 psi and 1400 °F).

of smooth ball against hard WC phase, especially within the area of rough waves, as shown in Fig. 8. Detachment of material from ball surface evidenced the material transfer from ball to coating surface, which is well also supported by overall EDS analysis of worn surface and wear debris in Fig. 10.

The residual stresses due to the KM™ coating process play a substantial role in assessing the wear performance of the current coatings. Within this aspect, tensile stresses within the coating deleteriously affect the wear properties [49,50]. However, Table 2 indicates that the KM™ WC-Co coatings were in a compressive stress state. Oladijo et al. [51] correlated residual stresses and abrasive wear behaviour of the WC-17Co HVOF coatings and reported that residual stresses developed post-spraying and during the wear testing are important for understanding their overall effect on wear resistance. High magnitude of compressive residual stresses resulted into improvement in wear resistance indicating a proportional relation between compressive residual stresses and abrasive wear resistance. In the current study, the residual stresses in as-sprayed state measured using neutron diffraction method were compressive in nature but exhibited disparity in their values due to use of different spray processing conditions. Combinatorial analysis of wear rate and as-sprayed residual stress mentioned in Table 2 and Table 5 demonstrated that 0.621 MPa and 760 °C (90 psi and 1400 °F) WC-Co coating with high compressive residual stresses exhibited lowest volume wear rate, i.e. high wear resistance. Whereas, the 0.414 MPa and 980 °C (60 psi and 1800 °F) coating with lower magnitude of compressive residual stresses exhibited lower wear resistance. However, in order to fully understand the relation between residual stresses and wear behaviour, residual stresses needed to be quantified after wear testing as well, which is currently beyond the scope for present study. Nonetheless, as a conclusion, in addition to the high hardness, low binder mean free path and oxide layer formation, compressive residual stresses stimulate the overall wear resistance of the KM™ WC-Co coatings. Therefore, even with high binder content (~35 wt% Co), the wear behaviour of KM™ processed WC-Co based coatings was as consistent and uniform as conventionally produced low binder content WC-Co coatings.

4. Conclusions

This work characterizes WC-Co coatings sprayed by the KM™ cold spray technique. All coatings exhibited a high density, uniform microstructure with less than 2% porosity and an absence of phase transformations. High energy impact of feedstock particles resulted in significant plastic deformation and particle penetration into the substrate. Furthermore, microhardness and elastic modulus with different spray parameters obtained were greater than 7.5 GPa and 140 GPa, respectively. The residual stress profile analysis of these KM™ WC-Co coatings revealed the presence of compressive residual macro-stress within the coating of magnitudes above 100 MPa. This stress was thermal in nature due to CTE mismatch between the WC-Co coating and the steel substrate. A tensile stress zone exists to a depth of approximately 0.5 mm under the substrate surface and can be associated with a thermal treatment process.

Micro-stresses, which are predominantly thermal in nature, are developed in the WC and Co phases due to the composite structure of the coating material. These micro-stresses are compressive for WC and tensile in Co; however, anisotropy was evident due to the anisotropic microcracking behaviour. The thermal nature of the micro-stress is supported by evaluation of the thermally generated stress that is based on composite theory.

The knowledge of stresses generated during the KM™ coating process and their linkage with other properties and production parameters is essential for the quality control of these critical structures. The stress formation mechanisms for the macro- and micro-stresses are related to the microstructure, micro-cracking, and mechanical properties. Understanding these properties allows prediction of the properties for further process and materials optimizations.

The KM™ deposited WC-Co coatings, even with high binder content (~35 wt% Co), exhibited equivalent wear resistance to conventionally produced low binder content WC-Co coatings. The wear behaviour of the coating was enhanced due to (i) forming a dense coating without any

phase transformation, (ii) a low mean free binder path, (iii) high hardness, (iv) overall compressive residual stress state, and (v) development of a wear inhibitive oxide layer. Hence, favorable residual stress formation in conjunction with superior mechanical properties promotes Kinetic Metallization™ as a process of industrial significance, especially for composite coatings.

CRediT authorship contribution statement

Ashok Meghwal: Conceptualization, Methodology, Validation, Formal analysis, Investigation, Writing – original draft, Visualization. **Christopher C. Berndt:** Conceptualization, Writing – review & editing, Visualization, Supervision, Funding acquisition. **Vladimir Luzin:** Methodology, Validation, Formal analysis, Investigation, Writing – original draft, Visualization. **Christiane Schulz:** Validation, Investigation, Writing – review & editing. **Travis Crowe:** Validation, Investigation, Resources. **Howard Gabel:** Validation, Investigation, Resources. **Andrew S.M. Ang:** Conceptualization, Methodology, Writing – review & editing, Visualization, Supervision, Funding acquisition.

Declaration of competing interest

The authors declare that they have no known competing financial interests or personal relationships that could have appeared to influence the work reported in this paper.

Acknowledgements

This study was supported by the Australian Research Council (ARC) under the Industrial Transformation Training Centre project IC180100005 that is titled “Surface Engineering for Advanced Materials”, SEAM. The authors acknowledge the Australian Centre for Neutron Scattering for their support in granting beam line time under proposal 5836. This work was performed in part at the South Australian node of the Australian National Fabrication Facility under the National Collaborative Research Infrastructure Strategy (NCRIS).

References

[1] A.S.M. Ang, C.C. Berndt, P. Cheang, Deposition effects of WC particle size on cold sprayed WC-Co coatings, Surf. Coat. Technol. 205 (10) (2011) 3260–3267.
[2] R.M. Tapphorn, H. Gabel, J.A. Henness, Kinetic metallizationTM of tungsten carbide-cobalt (WC-Co) coatings, Proceedings from the Materials Science & Technology (2005) 87–90.
[3] L. Pawlowski, The Science and Engineering of Thermal Spray Coatings: Second Edition, John Wiley and Sons, 2008.
[4] H.L. De Villiers Lovelock, Powder/processing/structure relationships in WC-Co thermal spray coatings: a review of the published literature, J. Therm. Spray Technol. 7 (3) (1998) 357–373.
[5] D.L. Gilmore, R.C. Dykhuizen, R.A. Neiser, T.J. Roemer, M.F. Smith, Particle velocity and deposition efficiency in the cold spray process, J. Therm. Spray Technol. 8 (4) (1999) 576–582.
[6] X.-T. Luo, C.-X. Li, F.-L. Shang, G.-J. Yang, Y.-Y. Wang, C.-J. Li, High velocity impact induced microstructure evolution during deposition of cold spray coatings: a review, Surf. Coat. Technol. 254 (2014) 11–20.
[7] H. Gabel, Kinetic metallization compared with HVOF, Adv. Mater. Process. 162 (5) (2004) 47–48.
[8] Y.K. Han, N. Birbilis, K. Spencer, M.X. Zhang, B.C. Muddle, Investigation of Cu coatings deposited by kinetic metallization, Mater. Charact. 61 (11) (2010) 1167–1186.
[9] B. Roebuck, Extrapolating hardness-structure property maps in WC/Co hardmetals, Int. J. Refract. Met. Hard Mater. 24 (1) (2006) 101–108.
[10] M. Couto, S. Dosta, M. Torrell, J. Fernández, J.M. Guilemany, Cold spray deposition of WC–17 and 12Co cermets onto aluminum, Surf. Coat. Technol. 235 (2013) 54–61.
[11] M. Couto, S. Dosta, J.M. Guilemany, Comparison of the mechanical and electrochemical properties of WC-17 and 12Co coatings onto Al7075-T6 obtained by high velocity oxy-fuel and cold gas spraying, Surf. Coat. Technol. 268 (2015) 180–189.
[12] R.M. Tapphorn, H. Gabel, System and Process for Solid-state Deposition and Consolidation of High Velocity Powder Particles using Thermal Plastic Deformation, Patent 6,915,964 B2, United States Patent and Trademark Office, 2002.
[13] R.M. Tapphorn, Howard Gabel, Powder Fluidizing Devices and Portable Powder-deposition Apparatus for Coating and Spray Forming, Patent 6,715,640, United States Patent and Trademark Office, 2004.
[14] ASTM E1920-03 (2014), Standard Guide for Metallographic Preparation of Thermal Sprayed Coatings, ASTM International, West Conshohocken, PA, 2014.
[15] ASTM C1327-15 (2019), Standard Test Method for Vickers Indentation Hardness of Advanced Ceramics, ASTM International, West Conshohocken, PA, 2019.
[16] W.C. Oliver, G.M. Pharr, Measurement of hardness and elastic modulus by instrumented indentation: advances in understanding and refinements to methodology, J. Mater. Res. 19 (1) (2004) 3–20.
[17] O. Kirstein, V. Luzin, U. Garbe, The strain-scanning diffractometer Kowari, Neutron News 20 (4) (2009) 34–36.
[18] V. Luzin, A. Valarezo, S. Sampath, Through-thickness residual stress measurement in metal and ceramic spray coatings by neutron diffraction, Mater. Sci. Forum 571-572 (2008) 315–320.
[19] A.M. Venter, V. Luzin, O.P. Oladijo, L.A. Cornish, N. Sacks, Study of interactive stresses in thin WC-Co coating of thick mild steel substrate using high-precision neutron diffraction, Mater. Sci. Forum 772 (2014) 161–165.
[20] P.H. Shipway, D.G. McCartney, T. Sudaprasert, Sliding wear behaviour of conventional and nanostructured HVOF sprayed WC–Co coatings, Wear 259 (7) (2005) 820–827.
[21] S. Matthews, J. Ansbro, C.C. Berndt, A.S.M. Ang, Carbide dissolution in WC-17Co thermal spray coatings: part 1-project concept and as-sprayed coatings, J. Alloys Compd. 856 (2020), 157464.
[22] X.-T. Luo, G.-J. Yang, C.-J. Li, Multiple strengthening mechanisms of cold-sprayed cBNp/NiCrAl composite coating, Surf. Coat. Technol. 205 (20) (2011) 4808–4813.
[23] E.O. Hall, The deformation and ageing of mild steel: III discussion of results, Proc. Phys. Soc. London Sect. B 64 (9) (1951) 747–753.
[24] N.J. Petch, The cleavage strength of polycrystals, J. Iron Steel Inst. 174 (1953) 25–28.
[25] A. Chaudhuri, Y. Raghupathy, D. Srinivasan, S. Suwas, C. Srivastava, Microstructural evolution of cold-sprayed Inconel 625 superalloy coatings on low alloy steel substrate, Acta Mater. 129 (2017) 11–25.
[26] S. Dosta, G. Bolelli, A. Candeli, L. Lusvarghi, I.G. Cano, J.M. Guilemany, Plastic deformation phenomena during cold spray impact of WC-Co particles onto metal substrates, Acta Mater. 124 (2017) 173–181.
[27] N. Huber, J. Heerens, On the effect of a general residual stress state on indentation and hardness testing, Acta Mater. 56 (20) (2008) 6205–6213.
[28] A.M. Venter, O.P. Oladijo, V. Luzin, L.A. Cornish, N. Sacks, Performance characterization of metallic substrates coated by HVOF WC–Co, Thin Solid Films 549 (2013) 330–339.
[29] R.A. Winholtz, Separation of Microstresses and Macrostresses, in: NATO ASI Series (Series E: Applied Sciences), Springer, 1992, pp. 131–145.
[30] V. Luzin, J. Matejicek, T. Gnaupel-Herold, Through-thickness residual stress measurement by neutron diffraction in Cu+W plasma spray coatings, Mater. Sci. Forum 652 (2010) 50–56.
[31] Y.C. Tsui, T.W. Clyne, An analytical model for predicting residual stresses in progressively deposited coatings part 1: planar geometry, Thin Solid Films 306 (1) (1997) 23–33.
[32] V. Luzin, K. Spencer, M. Zhang, N. Matthews, J. Davis, M. Saleh, Residual stresses in cold spray coatings, in: P. Cavaliere (Ed.), Cold-spray coatings: Recent trends and future perspective, Springer International Publishing, 2018, pp. 451–480.
[33] V. Luzin, A. Vackel, A. Valarezo, S. Sampath, Neutron through-thickness stress measurements in coatings with high spatial resolution, Mater. Sci. Forum 905 (2017) 165–173.
[34] V. Luzin, D. Fraser, Neutron through-thickness stress measurements in two-phase coatings with high spatial resolution, Mater. Res. Proc. 4 (2018) 111–116.
[35] V. Luzin, K. Spencer, M.X. Zhang, N. Matthews, Residual stress in coatings produced by cold spray, Mater. Sci. Forum 772 (2014) 155–159.
[36] D. Boruah, Theoretical prediction of residual stresses induced by cold spray with experimental validation, Multidiscip. Model. Mater. Struct. 15 (3) (2019) 599–616.
[37] D. Boruah, B. Ahmad, T.L. Lee, S. Kabra, A.K. Syed, P. McNutt, M. Doré, X. Zhang, Evaluation of residual stresses induced by cold spraying of Ti-6Al-4V on Ti-6Al-4V substrates, Surf. Coat. Technol. 374 (2019) 591–602.
[38] L.M. Berger, Application of hardmetals as thermal spray coatings, Int. J. Refract. Met. Hard Mater., 49, 350–364 (2015) (in English).
[39] A.S.M. Ang, WC-Co Coatings by Cold Spray Deposition for Replacing Hard Chrome in Industrial Applications, National University of Singapore, 2008.
[40] S. Dosta, M. Couto, J.M. Guilemany, Cold spray deposition of a WC-25Co cermet onto Al7075-T6 and carbon steel substrates, Acta Mater. 61 (2) (2013) 643–652.
[41] M. Couto, S. Dosta, J. Fernández, J.M. Guilemany, Comparison of the mechanical and electrochemical properties of WC-25Co coatings obtained by high velocity oxy-fuel and cold gas spraying, J. Therm. Spray Technol. 23 (8) (2014) 1251–1258.
[42] Q. Yang, T. Senda, A. Ohmori, Effect of carbide grain size on microstructure and sliding wear behavior of HVOF-sprayed WC–12% Co coatings, Wear 254 (1) (2003) 23–34.
[43] A. Mateen, G.C. Saha, T.I. Khan, F.A. Khalid, Tribological behaviour of HVOF sprayed near-nanostructured and microstructured WC-17wt.%Co coatings, Surf. Coat. Technol. 206 (6) (2011) 1077–1084.
[44] P. Mi, F. Ye, Structure and wear performance of the atmospheric heat-treated HVOF sprayed bimodal WC-Co coating, Int. J. Refract. Met. Hard Mater., 76, 185–191 (2018) (in English).
[45] J.A. Picas, Y. Xiong, M. Punset, L. Ajdelsztajn, A. Forn, J.M. Schoenung, Microstructure and wear resistance of WC-Co by three consolidation processing techniques, Int. J. Refract. Met. Hard Mater., 27(2), 344–349 (2009) (in English).

[46] B. Song, J.W. Murray, R.G. Wellman, Z. Pala, T. Hussain, Dry sliding wear behaviour of HVOF thermal sprayed WC-Co-Cr and WC-CrxCy-Ni coatings, Wear, 442–443, 203114, (2020) (in English).
[47] H. Saito, A. Iwabuchi, T. Shimizu, Effects of Co content and WC grain size on wear of WC cemented carbide, Wear 261 (2) (2006) 126–132.
[48] G. Bolelli, L.M. Berger, T. Börner, H. Koivuluoto, L. Lusvarghi, C. Lyphout, N. Markocsan, V. Matikainen, P. Nylén, P. Sassatelli, R. Trache, P. Vuoristo, Tribology of HVOF- and HVAF-sprayed WC–10Co4Cr hardmetal coatings: a comparative assessment, Surf. Coat. Technol. 265 (2015) 125–144.
[49] H. Liao, B. Normand, C. Coddet, Influence of coating microstructure on the abrasive wear resistance of WC/Co cermet coatings, Surf. Coat. Technol. 124 (2) (2000) 235–242.
[50] A. Meghwal, A. Anupam, V. Luzin, C. Schulz, C. Hall, B.S. Murty, R.S. Kottada, C. C. Berndt, A.S.M. Ang, Multiscale mechanical performance and corrosion behaviour of plasma sprayed AlCoCrFeNi high-entropy alloy coatings, J. Alloys Compd. 854 (2021), 157140.
[51] O.P. Oladijo, A.M. Venter, L.A. Cornish, Correlation between residual stress and abrasive wear of WC–17Co coatings, Int. J. Refract. Met. Hard Mater. 44 (2014) 68–76.